

# DM3D: Deformable Mamba via Offset-Guided Differentiable Scanning for Point Cloud Understanding

Bin Liu

School of Opto-electronical Engineering, Xi'an  
Technological University  
Xi'an, Shan'xi, China  
liubin@st.xatu.edu.cn

Xuelian Liu

Xi'an Key Laboratory of Active Photoelectric Imaging  
Detection Technology  
Xi'an, China  
liuxuelian@xatu.edu.cn

Chunyang Wang\*

Xi'an Key Laboratory of Active Photoelectric Imaging  
Detection Technology  
Xi'an, China  
Wangchunyang@xatu.edu.cn

Ge Zhang

School of Opto-electronical Engineering, Xi'an  
Technological University  
Xi'an, China  
zhangge@st.xatu.edu.cn

## Abstract

State Space Models (SSMs) show significant potential for long-sequence modeling, but their reliance on input order conflicts with the irregular nature of point clouds. Existing approaches often rely on predefined serialization schemes whose fixed scanning patterns cannot adapt to diverse geometric structures. To address this limitation, we propose DM3D, a deformable Mamba architecture for point cloud understanding. Specifically, DM3D introduces an offset-guided differentiable scanning mechanism that jointly performs resampling and reordering. Deformable Spatial Resampling (DSR) enhances structural awareness by adaptively resampling local features, while the Gaussian-based Differentiable Reordering (GDR) enables end-to-end optimization of the serialization order. We further introduce a Continuity-Aware State Update (CASU) mechanism that modulates the state update based on local geometric continuity. In addition, a Tri-Path Fusion module facilitates complementary interactions among different SSM branches. Together, these designs enable structure-adaptive serialization for point clouds. Extensive experiments on benchmark datasets show that DM3D achieves state-of-the-art or highly competitive results on classification, few-shot learning, and part segmentation tasks, validating the effectiveness of adaptive serialization for point cloud understanding.

## CCS Concepts

• **Computing methodologies** → **Shape analysis**; *Point-based models*; *Computer vision*.

## Keywords

3D Vision, Point Cloud, State Space Model, Deformable

## 1 Introduction

3D point clouds serve as a sparse yet efficient representation of real-world geometry and are widely used in various vision and multimedia applications, such as autonomous driving [47, 58, 61], robotics [7], AR/VR [15, 26], and immersive multimedia content creation [9]. Unlike structured 2D images, point clouds lack a regular grid structure, meaning there is no inherent spatial adjacency between points,

\*Corresponding author.

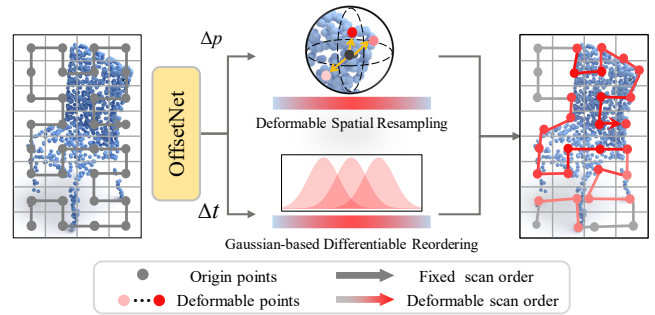


**Figure 1: Illustration of our deformable scanning. The offset network predicts spatial offsets  $\Delta p$  and sequential offsets  $\Delta t$ . These offsets guide differentiable spatial resampling and sequence reordering, yielding structure-aware representations that preserve fine-grained geometric details.**

which poses fundamental challenges to representation learning and semantic understanding [5, 25, 48, 62, 65]. Recently, Mamba [16] has advanced State Space Models (SSMs) [18] by introducing a selective mechanism, achieving remarkable computational efficiency and strong long-sequence modeling capability. However, applying Mamba to point clouds requires a crucial step—serialization—which plays a key role in the model’s ability to capture the underlying spatial structure.

A variety of strategies have been explored to construct sequences for point cloud sequential modeling, including space-filling curves (SFCs) [24, 25, 39, 55, 62], learned projection-based ordering [19, 28, 57], and voxel- or graph-based structural unfoldings [10, 46]. Although some of these methods exploit geometric structure during building, the resulting token order remains fixed once constructed and is not optimized with the downstream task. Such rigidity facilitates sequential processing in SSMs but fundamentally contradicts the irregular and permutation-invariant nature of point clouds [37, 38]. Consequently, spatially adjacent points may be scattered throughout the sequence, disrupting local continuity and hindering the capture of meaningful structural details, especially in sparse or complex regions. In contrast, human vision adaptively attends to

geometric edges, local details, and structural cues, extracting the most informative patterns with limited attention. Such selective perception efficiently builds discriminative and relational representations. Inspired by human visual attention, we argue that dynamically adjusting the scanning path according to the geometric structure is key to endowing SSMs with structural awareness.

While recent work such as DefMamba [29] has introduced deformable mechanisms into SSMs, its design is confined to the regular grids of 2D images, where scanning mainly amounts to reordering predefined token indices [21, 31, 54, 67]. More importantly, its sorting remains essentially discrete and is not directly differentiable. As a result, it explicitly requires manually designed gradient approximations for its non-differentiable operations. Point clouds, conversely, lack an inherent order. This means that a direct extension of 2D deformable Mamba to 3D is structurally incompatible. For point clouds, deformable scanning is not merely a simple matter of discrete token shuffling, but a structure-aware sequence construction problem that requires joint spatial adaptivity and adaptive serialization.

To address this challenge, we propose **DM3D (Deformable Mamba for 3D point clouds)**, which, to our knowledge, is the first deformable Mamba architecture tailored for point clouds. Rather than treating serialization as a discrete reordering procedure, DM3D reformulates it as a Gaussian-based continuous mapping. Specifically, learned spatial offsets guide the aggregation of local geometric neighborhoods, while learned sequential offsets assign token features to nearby positions in the sequence (see Fig. 1). Both processes allow gradients to flow directly to the corresponding offsets. In this way, DM3D turns serialization into a continuous optimization process, enabling the model to jointly learn where to sample and how to adapt the scan sequence according to the geometry. Our key contributions are as follows:

- We propose DM3D, which introduces deformable mechanisms into Mamba for point clouds through continuous and differentiable sequence construction, instead of relying on discrete token reordering.
- We design an offset-guided deformable scan that jointly performs Deformable Spatial Resampling (DSR) and Gaussian-based Differentiable Reordering (GDR), enabling geometry-aware local aggregation and end-to-end optimization of the sequence construction process.
- We introduce a Continuity-Aware State Update (CASU) mechanism and a Tri-Path Fusion (TPF) module to preserve geometric continuity during state evolution and enhance complementary interactions among SSM branches.
- Extensive experiments on benchmark datasets demonstrate that DM3D achieves state-of-the-art or highly competitive performance across classification, few-shot learning, and part segmentation tasks.

## 2 Related Work

### 2.1 Serialization and Mamba for Point Clouds

Point cloud serialization aims to convert unordered point sets into structured sequences compatible with sequence models. Previous methods generate sequences based on predefined traversal rules and model them with Transformer-based architectures [10, 32, 50]. As

point cloud sequences become longer, Transformers [43] encounter significant computational bottlenecks. In contrast, Mamba can handle such sequences more efficiently due to its linear complexity [19, 34, 55, 56]. However, its effectiveness depends on preserving the proximity of semantically or spatially related points in the serialized sequence [23, 33, 55, 60]. Thus, serialization serves as a crucial bridge between point clouds and Mamba, and different serialization schemes may be better suited to different tasks.

PointMamba [25] employs Hilbert and transposed Hilbert curves for efficient sequence generation, preserving spatial locality and providing a simple yet effective baseline. PCM [62] introduces a consistent traversal strategy, which generates multiple sequence variants along different coordinate axes and improves local continuity using order prompts. VoxelMamba [60] serializes voxelized scenes using Hilbert curves to maintain neighborhood consistency, while GridMamba [55] fuses multiple SFCs and randomly alternates among them across layers to alleviate locality loss.

Despite their implementation differences, these methods still use fixed mapping rules. DM3D instead learns the serialization order during training, turning serialization into an adaptive process.

### 2.2 Deformable Mechanisms in Visual Tasks

Deformable mechanisms enable models to dynamically adjust their receptive fields according to input content [12, 27, 29, 41, 49, 51, 53]. The concept originated from DCN [12], which introduced learnable offsets to adapt the convolutional sampling locations. DAT [53] later extended this idea to the attention mechanism. In point cloud understanding, PointConv [49] incorporated deformable continuous convolution to handle non-uniform point distributions, while KPConv [41] further introduced learnable kernel displacements to better adapt to diverse local geometries. 3D-GCN [27] combined deformable kernels with graph convolution to achieve translation and scale invariance. CenterFormer [66] and PTv2 [51] applied deformable attention in 3D detection and segmentation, respectively, for efficient multi-scale feature aggregation and improved spatial alignment, achieving notable performance gains.

Previous deformable designs have enabled CNNs and Transformers to adaptively sample positions in the spatial domain. In contrast, DM3D does not merely introduce deformability into point cloud SSMs. It unifies resampling and reordering into a continuous and fully differentiable process, allowing the model to jointly adapt sampling positions and construct geometry-aware sequences. Such joint adaptation has been less explored in prior methods that only deform spatial sampling or rely on static serialization strategies.

## 3 Method

### 3.1 Preliminaries

State Space Models (SSMs) are sequence modeling frameworks derived from linear time-invariant systems in control theory, capturing dependencies through latent state transitions. To adapt SSMs for discrete sequence modeling, Structured SSMs (S4) [17] employ the Zero-Order Hold (ZOH) method for discretization, introducing a timescale parameter  $\Delta$ . The discretized equations are:

$$\bar{A} = \exp(\Delta A), \quad \bar{B} = (\Delta A)^{-1} (\exp(\Delta A) - I) \Delta B \quad (1)$$

$$h_t = \bar{A}h_{t-1} + \bar{B}u_t, \quad y_t = Ch_t \quad (2)$$

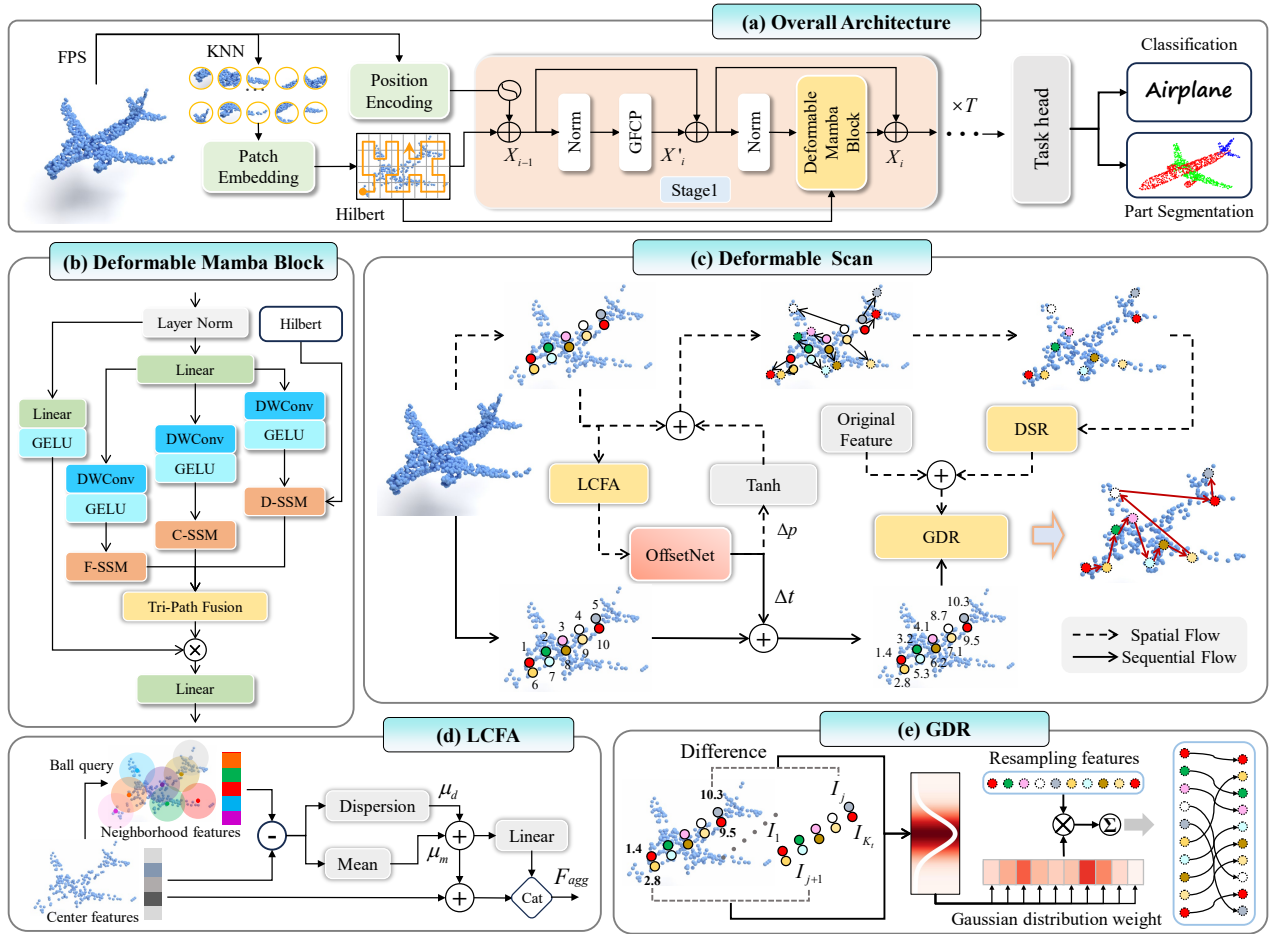


**Figure 2: Overview of DM3D.** (a) Overall architecture with the embedding, encoder, and task head. (b) The Deformable Mamba Block (DMB) consists of three SSM branches: a standard forward SSM [25] (F-SSM) branch, a channel-flip backward SSM [19] (C-SSM) branch, and a deformable SSM (D-SSM) branch. (c) Deformable Scan, the core of D-SSM, predicts spatial and sequential offsets via OffsetNet, enabling offset-guided spatial resampling and differentiable reordering. "Spatial flow" and "Sequential flow" indicate operations in the spatial and sequential domains, respectively. (d) LCFA provides local contextual cues for the offset network. (e) GDR performs differentiable token reordering according to learned offsets. Symbols:  $Cat$  denotes concatenation along the channel dimension,  $\odot$  element-wise multiplication,  $\ominus$  subtraction,  $\oplus$  residual addition,  $\otimes$  matrix multiplication, and  $\sum$  summation.

where  $\bar{A}$  and  $\bar{B}$  are the discretized counterparts of the continuous state transition matrix  $A$  and input projection matrix  $B$ , respectively.  $C$  denotes the output projection matrix, while  $u_t$ ,  $h_t$ , and  $y_t$  represent the input, hidden state, and output at time step  $t$ , respectively.

This discrete formulation enables SSMs to model long sequences with linear complexity. Mamba [16] enhances S4 through a Selective Scan (S6) mechanism that renders  $\Delta$ ,  $B$ , and  $C$  input-dependent, allowing for dynamic adjustment. This makes Mamba a robust and efficient framework for sequential processing.

### 3.2 Overview

DM3D adopts a ViT-style backbone architecture [22], following the design of baseline networks such as PointMamba [25] and Mamba3D [19]. The overall framework is illustrated in Fig. 2(a).

Given an input point cloud, we first apply Farthest Point Sampling (FPS) and K-Nearest Neighbor (KNN) grouping to partition it into  $N$  local groups, each containing  $K$  points. A lightweight PointNet extracts local features  $F \in \mathbb{R}^{N \times D}$ , and the corresponding group centers are denoted by  $P \in \mathbb{R}^{N \times 3}$ , where  $D$  is the embedding dimension. To inject geometric priors, the coordinates of each center are encoded by an MLP to obtain position embeddings  $P_{emb} \in \mathbb{R}^{N \times D}$ , which are then added to the local features. A classification token  $F_{CLS} \in \mathbb{R}^{1 \times D}$  is prepended, and the resulting embeddings are serialized using a Hilbert curve to form the initial token sequence  $X_0 \in \mathbb{R}^{(N+1) \times D}$  for subsequent modeling. Each encoder stage in DM3D follows a Transformer-like architecture consisting of a Geometry-Feature Coupled Pooling (GFPCP) module

and a Deformable Mamba Block (DMB). The GFPC module, introduced in HyMamba [28], serves as a local enhancement layer, while the Deformable Mamba Block performs deformable modeling. The computations at the  $i$ -th stage are formulated as follows:

$$X_i' = \text{GFPC}(\text{LN}(X_{i-1})) + X_{i-1} \quad (3)$$

$$X_i = \text{DMB}(\text{LN}(X_i')) + X_i' \quad (4)$$

where  $X_i \in \mathbb{R}^{(N+1) \times D}$  is the output of the  $i$ -th stage and  $\text{LN}$  denotes the Layer Normalization.

After  $T$  encoding stages, the final-stage features are fed into different task heads depending on the downstream task. For classification, we concatenate the classification token with the average-pooled feature as the final representation.

### 3.3 Deformable Mamba Block

The Deformable Mamba Block, the core of this work, aims to perform deformable scanning by modifying point positions and local scan order. As illustrated in Fig. 2(b), following prior works [29, 55, 56], we replace the original 1D causal convolution [3] with a depthwise convolution and introduce a D-SSM branch. Meanwhile, we retain the C-SSM branch from Mamba3D [19] and the F-SSM branch from PointMamba [25] to maintain model stability.

*Local Context Feature Aggregation (LCFA).* Pointwise representations in isolation are insufficient to capture fine-grained geometric structure, since geometric relationships in point clouds primarily reside within local neighborhoods. Therefore, meaningful offset prediction requires awareness of the surrounding geometric context. As illustrated in Fig. 2(d), we compute center-to-neighbor feature differences to capture local contextual and semantic variations with minimal overhead.

Formally, given a center point  $p_i \in P$  and its associated feature  $f_i \in \mathbb{R}^D$ , a ball query [37] identifies its local neighborhood  $\mathcal{N}(i) = \{p_j \mid |p_j - p_i| \leq r\}$ . The neighboring coordinates and features are denoted by  $P_{\mathcal{N}(i)} \in \mathbb{R}^{K_r \times 3}$  and  $F_{\mathcal{N}(i)} \in \mathbb{R}^{K_r \times D}$ , respectively, where  $K_r$  is the number of neighbors. For the central feature  $f_i$ , the relative feature discrepancy to a neighbor  $j \in \mathcal{N}(i)$  is defined as  $d_{ij} = f_j - f_i$ . Subsequently, we derive local feature statistics, namely the mean  $\mu_m$  and dispersion  $\mu_d$ , as follows:

$$\mu_m = \frac{1}{K_r} \sum_{j \in \mathcal{N}(i)} d_{ij}, \quad \mu_d = \frac{1}{K_r} \sum_{j \in \mathcal{N}(i)} |d_{ij}| \quad (5)$$

To guide offset prediction, we project the local statistics into a compact semantic subspace using a low-rank projection layer, yielding a lightweight semantic cue  $f_{sem} = \phi(|\mu_m| + \mu_d)$ . We then combine these local statistics with the center feature to replenish the holistic shape context:

$$f_{agg} = \text{Concat}(\mu_m + \mu_d + \alpha f_i; f_{sem}) \quad (6)$$

where  $f_{agg}$  denotes the aggregated feature for the center point, and stacking all  $f_{agg}$  yields the feature map  $F_{agg} \in \mathbb{R}^{N \times D}$ . Here,  $\alpha$  is a scaling coefficient used to preserve the contribution of the center feature. This design enables the offset network to capture fine-grained local variations while retaining semantic context.

*Offset-guided Gaussian Weighting.* Following DAT [53], we adopt a depthwise separable convolution [8] with a large kernel, followed by a channel attention (CA) [20, 29], a ReLU activation, and a  $1 \times 1$  convolution, to predict the initial four-dimensional offsets. To prevent excessively large deformations, the offsets are bounded by a hyperbolic tangent function and then decomposed into spatial and sequential components:

$$O_{offset} = \text{Conv}_{1 \times 1}(\text{ReLU}(\text{CA}(\text{DWConv}(F_{agg})))) \quad (7)$$

$$O'_{offset} = \tanh(O_{offset}) = [\Delta p; \Delta t] \quad (8)$$

where  $\Delta p \in \mathbb{R}^{N \times 3}$  represents spatial offsets for coordinate deformation, and  $\Delta t \in \mathbb{R}^{N \times 1}$  denotes sequential offsets for sequence reordering.

The offset operation produces sampled positions that no longer align with the original point set, thereby requiring both spatial resampling and sequential reordering. We observe that these two operations share a common principle: points with higher similarity should exert a stronger influence during feature aggregation and sequence reordering, while the contribution of dissimilar points should gradually decay. Motivated by this, we cast resampling and reordering into a common framework rather than treating them as entirely unrelated processes.

Specifically, we introduce a mechanism that applies Gaussian kernels with the same functional form in both the spatial and sequential domains, differing only in the corresponding distance measures and neighborhood definitions. This provides a common weighting principle for both resampling and reordering. The general Gaussian kernel is defined as:

$$\mathcal{W}(d; \sigma) = \exp\left(-\frac{d^2}{2\sigma^2}\right) \quad (9)$$

where  $d$  denotes either coordinate distance or index distance, and  $\sigma$  is the corresponding learnable scale parameter in each domain.

*Deformable Spatial Resampling (DSR).* For spatial resampling, after applying the coordinate offsets, each deformed point  $p'_i$  reuses the local neighbor index set  $\mathcal{N}(i) = \{j_1, \dots, j_{K_r}\}$  constructed by the initial ball query instead of performing a new neighbor search. This reduces overhead and preserves the local neighborhood consistency during feature aggregation. For each deformed point  $p'_i$ , feature interpolation is performed over its neighborhood  $\mathcal{N}(i)$ :

$$p'_i = p_i + \Delta p_i \quad (10)$$

$$f_i'^{(s)} = \sum_{j \in \mathcal{N}(i)} \frac{\mathcal{W}(\|p'_i - p_j\|_2; \sigma_s)}{\sum_{l \in \mathcal{N}(i)} \mathcal{W}(\|p'_i - p_l\|_2; \sigma_s) + \varepsilon} f_j \quad (11)$$

where  $p_j$  denotes a neighboring point,  $f_i'^{(s)}$  is the resampled feature,  $f_j$  is the neighbor feature associated with  $p_j$ ,  $\sigma_s$  is the scale parameter for spatial resampling, and  $\varepsilon$  is a small constant to avoid division by zero.

Notably, because point clouds lack a fixed grid structure, the network can learn directly from point coordinates without relying on a relative offset bias matrix [29, 53], thereby enabling more natural spatial deformation.

*Gaussian-based Differentiable Reordering (GDR)*. Traditional sorting explicitly reorders point indices, but its discrete nature blocks gradient flow and prevents end-to-end optimization [14, 29]. To overcome this issue, we model reordering as a continuous local assignment process and propose Gaussian-based Differentiable Reordering (GDR). As illustrated in Fig. 2(e), GDR maps each token to a Gaussian-weighted distribution over nearby sequence indices rather than a single discrete position, thereby enabling differentiable local reordering.

Specifically, we add the token offsets  $\Delta t$  to the base index vector  $I = [I_1, I_2, \dots, I_N]^T \in \mathbb{R}^{N \times 1}$  derived from the Hilbert curve, yielding the offset index value  $s_i$ . GDR restricts candidate targets to a local index window  $\Omega(i)$  centered at  $I_i$ , containing up to  $K_t$  candidate indices. For each token  $i$ , we compute the deviations between  $s_i$  and the discrete base indices  $I_j$  within  $\Omega(i)$ , and then perform Gaussian-weighted aggregation for differentiable local reordering:

$$s_i = I_i + \Delta t_i, \quad (12)$$

$$f_i^{(t)} = \sum_{j \in \Omega(i)} \frac{\mathcal{W}(s_i - I_j; \sigma_t)}{\sum_{l \in \Omega(i)} \mathcal{W}(s_i - I_l; \sigma_t) + \varepsilon} f_j^{(s)} \quad (13)$$

where  $f_i^{(t)}$  denotes the reordered feature of the  $i$ -th token,  $\sigma_t$  is the learnable scale parameter controlling the smoothness of local reordering, and  $f_j^{(s)}$  denotes the  $j$ -th feature after fusion of the resampled and original features.

During Gaussian-weighted aggregation, token features are assigned to neighboring sequence indices within the local index window, forming a continuous and differentiable relaxation of discrete sorting. Importantly, GDR does not rely on non-differentiable sorting; instead, it provides a continuous relaxation of local discrete reordering (see Appendix for details):

- As  $\sigma_t \rightarrow 0^+$ , the mapping approaches deterministic local reassignment, where each offset index  $s_i$  is assigned to the closest discrete base index  $I_j$  within  $\Omega(i)$ . The reordered token feature approaches that of its nearest local candidate.
- For any fixed  $\sigma_t > 0$ , the normalized Gaussian weights remain continuous and differentiable with respect to  $s_i$ , enabling smooth gradient propagation and end-to-end optimization.
- As  $\sigma_t \rightarrow +\infty$ , GDR degenerates into local average pooling over the candidate window, with gradients vanishing as the derivative converges to zero everywhere.

As  $\sigma_t$  decreases, the reassignment gradually approaches hard local assignment, whereas as  $\sigma_t$  increases, GDR gradually degenerates into local average pooling. This allows deformable scanning to approximate discrete order adjustment in a differentiable manner, thereby preserving end-to-end optimization of the serialization order. By jointly learning offsets in both spatial and sequential domains, DM3D adaptively refines point coordinates and scan order, leading to better adaptation to geometric structure in point cloud.

### 3.4 State Update and Path Fusion Mechanisms

*Continuity-Aware State Update*. Linearizing unordered point clouds into 1D sequences inevitably disrupts spatial continuity. Although DSR and GDR adapt the scan order to better align the serialized sequence with local structure, neighboring tokens in the reordered

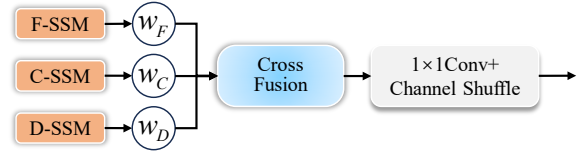


Figure 3: Illustration of TPF.

sequence may still be discontinuous in 3D space. Standard SSMs predict the update step size ( $\Delta$ ) solely from feature cues, without considering whether adjacent tokens are truly spatially adjacent. As a result, points that are adjacent in the sequence but distant in 3D space may still exchange information, while truly neighboring points may interact insufficiently. We therefore propose the Continuity-Aware State Update (CASU) mechanism, which incorporates geometric continuity into state evolution to stabilize feature propagation in the deformable sequence.

We compute the Euclidean distance between consecutive points  $p_{i-1}$  and  $p_i$  in the deformed coordinates after applying spatial offsets, and use it as a cue of geometric continuity. This distance is used to define a scaling factor  $\phi$  that modulates the original step size  $\Delta_i$ , yielding the geometry-aware step  $\Delta'_i$ :

$$\Delta'_i = \Delta_i \cdot \phi = \Delta_i \cdot (1 + \tanh(\|p_i - p_{i-1}\|_2)) \quad (14)$$

A larger spatial distance between consecutively scanned points results in a larger  $\Delta'_i$ . This causes the previous state to decay more rapidly through  $A$ , and relatively increases the influence of the current input via  $B$ . Consequently, undesired information propagation between geometrically discontinuous points is suppressed. To avoid excessive suppression of long-range correlations, CASU is applied only to the D-SSM branch, while long-range context is still preserved by the parallel F-SSM and C-SSM branches.

*Tri-Path Fusion*. In the DMB, the F-SSM, C-SSM, and D-SSM capture features through different modeling pathways. However, these paths may encode overlapping information, leading to redundancy. To mitigate this, we introduce a lightweight cross-path interaction that lets each path reweight the others, thereby reducing redundancy and enhancing complementarity (see Fig. 3).

The three branch features,  $F_F, F_C, F_D \in \mathbb{R}^{N \times D}$ , are first adaptively modulated by the other two branches before fusion:

$$w_i = \text{sigmoid}(F_i), \quad F'_i = F_i \odot \frac{1}{2}(w_j + w_k) \quad (15)$$

where  $(i, j, k)$  cycles over  $(F, C, D)$ ,  $(C, D, F)$ , and  $(D, F, C)$ .

This enables each pathway to perceive the activation strength of the others, allowing dynamic adjustment of their relative importance. The modulated features are concatenated along the channel dimension and fused by a grouped convolution (GConv), reducing the feature dimension back to  $D$ . To maintain inter-group communication, channel shuffle [64] is applied after fusion:

$$F_{out} = \text{Shuffle}(\text{GConv}_{1 \times 1}([F'_F; F'_C; F'_D])) \quad (16)$$

**Table 1: Classification on ModelNet40 and ScanObjectNN. We report overall accuracy (%), number of parameters(#P), and FLOPs (#F). We use *rotation* and *scale&translate* as data augmentation for ScanObjectNN and ModelNet40, respectively.**

Reference	Methods	ScanObjectNN			ModelNet40 (1k pts)		#P (M)	#F (G)
		OBJ_BG	OBJ_ONLY	PB_T50_RS	w/o Vote	w/ Vote		
<i>Supervised Learning Only</i>								
CVPR 17	PointNet [5]	73.3	79.2	68.0	89.2	-	3.5	0.5
NeurIPS 17	PointNet++ [37]	82.3	84.3	77.9	90.7	-	1.5	1.7
TOG 19	DGCNN [48]	82.8	86.2	78.1	92.9	-	1.8	2.4
NeurIPS 22	PointNeXt [38]	-	-	87.7	92.9	-	1.4	3.6
JAS 23	PointConT [30]	-	-	88.0	93.5	-	-	-
NeurIPS 24	PointMamba [25]	88.30	87.78	82.48	-	-	12.3	3.6
ACM MM 25	HydraMamba [39]	-	-	88.3	<b>94.0</b>	-	-	-
CVPR 25	SAST [2]	92.25	91.39	87.30	92.7	-	12.3	3.6
AAAI 25	PCM [62]	-	-	88.1	93.4	-	34.2	45.0
	DM3D	<b>93.11</b>	<b>91.74</b>	<b>90.83</b>	<b>94.0</b>	-	18.6	4.0
<i>With Self-supervised Pre-training</i>								
CVPR 22	Point-BERT [57]	87.43	88.12	83.07	92.7	93.2	23.8	4.8
ECCV 22	Point-MAE [35]	92.77	91.22	89.04	92.7	93.8	23.8	4.8
NeurIPS 23	PointGPT-S [6]	93.39	92.43	89.17	93.3	94.0	29.2	5.7
AAAI 24	Point-FEMAE [59]	<b>95.18</b>	93.29	90.22	94.0	94.5	27.4	3.6
NeurIPS 24	PointMamba [25]	94.32	92.60	89.31	93.6	94.1	12.3	3.6
ACM MM 24	Mamba3D [19]	93.12	92.08	92.05	94.7	95.1	16.9	3.9
CVPR 25	SAST [2]	94.32	91.91	89.10	93.4	-	12.3	3.6
ICCV 25	StruMamba3D [44]	95.18	93.63	92.75	<b>95.1</b>	<b>95.4</b>	15.8	4.0
ICCV 25	Point-PQAE [63]	95.0	93.6	89.6	94.0	-	22.1	-
	DM3D	94.71	<b>93.83</b>	<b>93.30</b>	94.9	95.2	18.6	4.0

## 4 Experiments

### 4.1 Implementation Details

All experiments are conducted on a single NVIDIA TITAN RTX 24GB GPU. We set the total number of stages  $T$  to 12, the hidden dimension  $D$  to 384, the number of points sampled by FPS to  $N = 128$ , and the number of neighbors in KNN to  $K = 32$ . For DSR and GDR,  $K_r$  and  $K_t$  are set to 4 and 9, while  $\sigma_s$  and  $\sigma_t$  are initialized to 1 and 0.2, respectively. The models are trained for 300 epochs using the AdamW optimizer with the cosine learning rate scheduler (CosLR), an initial learning rate of  $5e-4$ , a weight decay of 0.05, 10 warmup epochs, and batch size of 32. The pre-training is conducted on ShapeNetCore [4], following Point-MAE protocols [19, 25, 35], see Appendix for more implementation and pre-training details.

### 4.2 Downstream Tasks

*Classification.* We use a three-layer MLP as the classification head and evaluate our DM3D on ModelNet40 [52] and ScanObjectNN [42]. ModelNet40 uses 1024 input points with scale&translate augmentation, while ScanObjectNN uses 2048 points with rotation augmentation. As shown in Tab. 1, DM3D achieves highly competitive results. Without pre-training, it achieves 94.0% on ModelNet40 and 90.83% on PB\_T50\_RS, outperforming recent Mamba variants such as SAST [2] and PCM [62], indicating strong robustness under perturbations. With pre-training, DM3D further improves PB\_T50\_RS overall accuracy (OA) to 93.30%, surpassing recent counterparts including StruMamba3D [44], Point-PQAE [63]

**Table 2: Few-shot classification on ModelNetFewShot.  $A_{\pm std}$  represents the average (A) and standard deviation (std) of OA.**

Methods	5-Way		10-Way	
	10-Shot	20-Shot	10-Shot	20-Shot
<i>Supervised Learning Only</i>				
PointNet [5]	52.0 $\pm$ 3.8	57.8 $\pm$ 4.9	46.6 $\pm$ 4.3	35.2 $\pm$ 4.8
DGCNN [48]	31.6 $\pm$ 2.8	40.8 $\pm$ 4.6	19.9 $\pm$ 2.1	16.9 $\pm$ 1.5
OcCo [45]	90.6 $\pm$ 2.8	92.5 $\pm$ 1.9	82.9 $\pm$ 1.3	86.5 $\pm$ 2.2
DM3D	<b>91.1<math>\pm</math>5.2</b>	<b>95.0<math>\pm</math>2.9</b>	<b>86.1<math>\pm</math>4.6</b>	<b>92.0<math>\pm</math>1.8</b>
<i>With Self-supervised Pre-training</i>				
ACT [13]	96.8 $\pm$ 2.3	98.0 $\pm$ 1.4	93.3 $\pm$ 4.0	95.6 $\pm$ 2.8
Point-BERT [57]	94.6 $\pm$ 3.1	96.3 $\pm$ 2.7	91.0 $\pm$ 5.4	92.7 $\pm$ 5.1
Point-MAE [35]	96.3 $\pm$ 2.5	97.8 $\pm$ 1.8	<b>92.6<math>\pm</math>4.1</b>	95.0 $\pm$ 3.0
PointGPT-S [6]	<b>96.8<math>\pm</math>2.0</b>	<b>98.6<math>\pm</math>1.1</b>	92.6 $\pm$ 4.6	95.2 $\pm$ 3.4
PointMamba [25]	95.0 $\pm$ 2.3	97.3 $\pm$ 1.8	91.4 $\pm$ 4.4	92.8 $\pm$ 4.0
DM3D	96.1 $\pm$ 4.5	97.9 $\pm$ 2.3	91.4 $\pm$ 4.3	<b>95.8<math>\pm</math>3.0</b>

(Transformer-based, 89.6%), and SAST [2] (89.1%). The gain is most pronounced on PB\_T50\_RS, which indicates that adaptive scan construction improves robustness under perturbation. Moreover, DM3D remains significantly lighter than PCM [62] and somewhat lighter than Point-PQAE [63] in parameter count, while introducing only a minor computational overhead (+0.1G FLOPs) compared with the Mamba3D baseline [19].

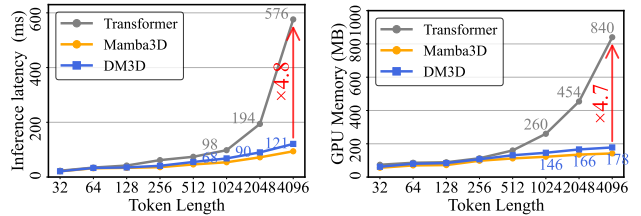
**Table 3: Part segmentation on ShapeNetPart. We report class-level mIoU (mIoU<sub>C</sub>) and instance-level mIoU (mIoU<sub>I</sub>).**

Reference	Method	mIoU <sub>C</sub> (%)	mIoU <sub>I</sub> (%)
<i>Supervised Learning Only</i>			
CVPR 17	PointNet [5]	80.4	83.7
NeurIPS 17	PointNet++ [37]	81.9	85.1
TOG 19	DGCNN [48]	82.3	85.2
	<b>DM3D</b>	<b>83.7</b>	<b>85.3</b>
<i>With Self-supervised Pre-training</i>			
ECCV 22	Point-MAE [35]	84.2	86.1
CVPR 22	Point-BERT [57]	84.1	85.6
NeurIPS 23	PointGPT-S [6]	84.1	86.2
ICLR 23	ACT [13]	84.7	86.2
NeurIPS 24	PointMamba [25]	84.4	86.0
ACM MM 24	Mamba3D [19]	83.6	85.6
ICCV 25	Point-PQAE [63]	84.6	86.1
ICCV 25	StruMamba3D [44]	-	86.7
AAAI 26	CloudMamba [40]	-	86.6
	<b>DM3D</b>	<b>84.8</b>	<b>86.7</b>

*Few-shot Learning.* Following the standard N-way K-shot protocol and prior work [19, 25, 28, 57], we evaluate the few-shot learning capability of DM3D on the ModelNetFewShot benchmark. As shown in Tab. 2, DM3D consistently outperforms other methods under the supervised-only setting, demonstrating strong feature learning capability. With pre-training, DM3D remains competitive, though it does not achieve the best 10-shot results, possibly because it emphasizes structure-aware sequence modeling rather than semantic transfer from large-scale pre-training. When increased to 20-shot, DM3D achieves highly competitive performance, with a clear improvement over the 10-shot setting.

*Part Segmentation.* ShapeNetPart [4] contains 50 part categories across 16 object classes. We use 2048 input points without normals, and adopt a PointNet++-style [25, 37] segmentation head that aggregates features from the 4th, 8th, and 12th encoder layers. Tab. 3 shows that ShapeNetPart is extremely challenging, and even state-of-the-art methods only marginally improve compared to others. With pre-training, DM3D achieves 84.8% mIoU<sub>C</sub> and 86.7% mIoU<sub>I</sub>. This surpasses the PointMamba by 0.7%/0.4% in mIoU<sub>I</sub>/mIoU<sub>C</sub>, and matches or slightly outperforms recent methods such as Point-PQAE [63], StruMamba3D [44], and CloudMamba [40], suggesting that deformable design is beneficial for capturing fine-grained geometric details. See Appendix for more visual results.

*Efficiency Analysis.* We measure inference latency and peak GPU memory usage on an NVIDIA TITAN RTX with a batch size of 1. As shown in Fig. 4, the resource growth of DM3D is near-linear in practice. At  $N = 4096$ , it achieves  $\sim 4.8\times$  lower latency and  $\sim 4.7\times$  lower peak memory than Transformers, while closely following the Mamba3D trend. In the deformable scan, the feature differencing, DSR, and GDR are restricted to local regions, while the costs of offset prediction and path fusion grow linearly with  $N$  when  $D$  is fixed. Consequently, it introduces merely marginal  $\mathcal{O}(KN)$  overhead, while providing geometric adaptivity.

**Figure 4: Inference latency and peak GPU memory usage for a single sample.****Table 4: Ablation on model architecture and components of deformable scanning.**

Method	OBJ_ONLY	PB_T50_RS	#P (M)	#F (G)
<i>(a) Ablation on model architecture</i>				
★ Full	<b>91.7</b>	<b>90.8</b>	18.6	4.0
w/o D-SSM	88.5	85.7	16.9	3.8
w/o CASU	89.8	88.6	18.6	4.0
w/o TPF	90.9	89.0	18.5	4.0
<i>(b) Ablation on deformable scanning subcomponents</i>				
w/o LCFA	90.4	89.4	18.6	4.0
w/o OffsetNet	88.9	86.6	18.1	3.9
w/o DSR	89.3	88.6	18.6	4.0
w/o GDR	89.1	87.3	18.6	4.0

### 4.3 Ablation Studies

To evaluate each component, we conduct ablation studies on the overall architecture and deformable scanning modules, with all variants trained from scratch.

*Effect of Each Component.* As shown in Tab. 4, the full model consistently outperforms all ablated variants on both OBJ\_ONLY and PB\_T50\_RS. Ablating D-SSM, CASU, and TPF leads to clear performance degradation, with drops of 3.2%/5.1%, 1.9%/2.2%, and 0.8%/1.8%, respectively. This confirms that the deformable branch is the most critical component, while the state update and path fusion modules also provide smaller yet steady gains.

We further ablate the subcomponents of the deformable scanning module. Removing LCFA causes performance drops of 1.3% and 1.4% on OBJ\_ONLY and PB\_T50\_RS, respectively, indicating that neighborhood aggregation provides richer contextual cues for offset prediction. Removing OffsetNet causes the largest drops of 2.8% and 4.2%, since the model can neither perform spatial deformation nor adaptive reordering. Removing DSR disables local feature resampling after spatial deformation, leading to smaller drops of 2.4% and 2.2%, while removing GDR causes drops of 2.6% and 3.5%. These results validate the effectiveness of our design choices and demonstrate the contribution of each proposed component.

*Effect of reordering methods and scale  $\sigma_i$  in GDR.* As shown in Tab. 5(a), relying solely on a fixed Hilbert serialization yields the lowest performance, highlighting the necessity of dynamic sequence adjustment. Discrete reordering improves the results only marginally,

**Table 5: Ablation on key design choices. We evaluate the effects of reordering methods, the Gaussian scale  $\sigma_t$  in GDR, and different state update and path fusion strategies.**

Module	Setting	OBJ_ONLY	PB_T50_RS
<i>(a) Reordering methods and the Gaussian scale <math>\sigma_t</math> in GDR</i>			
Reordering variants	Fixed order (Hilbert)	90.07	88.62
	Discrete [36]	90.34	89.11
	Sinkhorn [11]	91.53	89.92
GDR (Ours)	$\sigma_t = 0.1$	91.49	89.82
	$\sigma_t = 0.2$	<b>91.74</b>	<b>90.83</b>
	$\sigma_t = 0.4$	91.37	89.79
	$\sigma_t = 0.6$	91.26	89.54
<i>(b) State update strategies.</i>			
State update	Linear Scaling	90.88	89.02
	Feature Similarity	90.01	88.23
	CASU (Ours)	<b>91.74</b>	<b>90.83</b>
<i>(c) Path fusion strategies.</i>			
Path fusion	Element-wise mean	91.51	89.73
	Convolution	91.48	89.80
	TPF (Ours)	<b>91.74</b>	<b>90.83</b>

indicating that discrete reassignment without gradient flow is insufficient for robust sequence refinement. Sinkhorn [11] and our GDR both benefit from end-to-end differentiability for gradient optimization, but GDR performs better. We attribute this to Sinkhorn imposing a more global assignment relaxation, whereas GDR restricts reassignment to a constrained local index window. This design explicitly preserves geometric adjacency and better matches the local structure of point clouds, thereby enabling more effective adjustment of the serialization order under perturbations.

Furthermore, we ablate the scale parameter  $\sigma_t$ , which controls the smoothness of the differentiable reordering in GDR. An overly small  $\sigma_t$  makes the reassignment nearly discrete and impedes smooth gradient propagation, whereas an overly large  $\sigma_t$  oversmooths local assignments and weakens discriminative structural cues. The optimal balance is achieved at  $\sigma_t = 0.2$ .

*Effect of CASU.* To validate the design of CASU, we compare it with two alternative modulation strategies: Linear Scaling (LS), which sets  $\phi = 2\|p_i - p_{i-1}\|_2$ , and Feature Similarity (FS), which sets  $\phi = 1 + [1 - \cos(f_i, f_{i-1})]/2$ . Here,  $p_{i-1}$  and  $p_i$  denote consecutive scanned points, and  $f_{i-1}$  and  $f_i$  denote their corresponding features. LS is a simple geometry-based baseline, while FS is a lightweight feature-based variant. They are used to test whether state updates should be guided by geometric continuity or feature cues.

As shown in Tab. 5(b), CASU achieves the best performance by using a bounded nonlinear modulation function. The Euclidean distance directly reflects whether two consecutive tokens remain spatially continuous after deformable scanning. Although LS utilizes this geometric distance, its unbounded linear scaling makes the state update overly sensitive to large spatial gaps. Meanwhile, the FS approach performs the worst, indicating that feature correlation does not reliably reflect true spatial continuity between adjacent

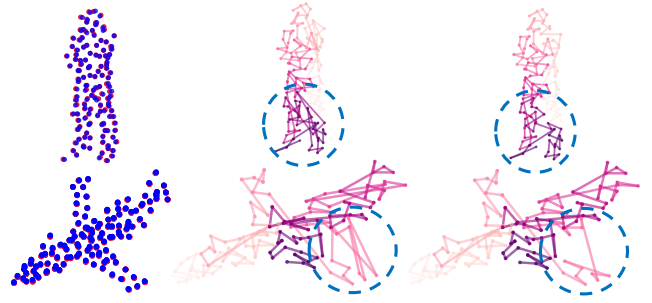


**Figure 5: Visualization of the deformable scanning mechanism. Left: coordinates (128 points) before deformation (blue) and after deformation (red). Middle: Hilbert curve scan order. Right: deformable scan order (darker denotes higher index).**

tokens. These results suggest that smoother, bounded geometry-guided modulation is more effective for state evolution in serialized point clouds than direct distance scaling or feature-based cues.

*Effect of fusion strategies.* As shown in Tab. 5(c), we compare different path fusion strategies. Simple Element-wise mean provides limited cross-branch interaction, while our TPF achieves better performance than convolutional fusion by enabling more effective information exchange across paths.

#### 4.4 Visualization and Discussion

To better illustrate the effect of deformable scanning, we provide a visual analysis in Fig. 5.

*Analysis of Coordinate Offset.* Larger offsets are observed near object boundaries in the left panel of Fig. 5, where geometric variations are richer. This indicates that larger spatial offsets are assigned to geometrically informative regions, guiding resampling toward them and thereby enhancing sensitivity to fine structural details.

*Analysis of Differentiable Reordering.* By design, DM3D performs sequence serialization via a continuous probabilistic mapping, where each token contributes to multiple sequence positions rather than being assigned to a single fixed discrete index. Still, visualizing the traversal order remains essential for intuitively understanding the scan’s structural adaptability. To achieve this, we apply an argmax projection to the assignment weights, obtaining an approximate discrete traversal order for interpretive visualization only.

As shown in the middle and right panels of Fig. 5, the Hilbert curve jumps across nearby but structurally distinct parts, such as between the wings and fuselage of the "airplane" or between separated limbs of the "person", resulting in reduced local continuity. In contrast, the deformable scan adaptively refines the base serialization according to local geometric context, causing points from the same object part to be visited more consecutively. As a result, DM3D preserves the overall stability of the base scan while achieving better local structural alignment, coherently traversing structurally related regions with fewer boundary crossings.

## 5 Conclusion

In this paper, we propose DM3D, a deformable Mamba network for point cloud understanding. Unlike prior methods constrained by predefined serialization, DM3D unifies spatial resampling and differentiable sequence reordering through an offset-guided deformable mechanism, enabling end-to-end optimization of both spatial sampling and scan order. Extensive experiments on ModelNet40, ScanObjectNN, and ShapeNetPart demonstrate highly competitive performance, suggesting that point cloud serialization benefits from being learned and adapted as part of the model rather than treated as a static preprocessing step. While effective, the current deformable reordering operates within local neighborhoods, which may limit long-range structural modeling. Future research will explore multi-scale or global deformable schemes to capture broader topological dependencies and enhance holistic shape understanding.

## References

- [1] Iro Armeni, Ozan Sener, Amir R. Zamir, Helen Jiang, Ioannis Brilakis, Martin Fischer, and Silvio Savarese. 2016. 3D Semantic Parsing of Large-Scale Indoor Spaces. In *Proc. IEEE/CVF Conference on Computer Vision and Pattern Recognition (CVPR)*. 1534–1543.
- [2] Ali Bahri, Moslem Yazdanpanah, Mehrdad Noori, Sahar Dastani, Milad Cheraghlikhani, Gustavo Adolfo Vargas Hakim, David Osowiecki, Farzad Bezaee, Ismail Ben Ayed, and Christian Desrosiers. 2025. Spectral Informed Mamba for Robust Point Cloud Processing. In *Proc. IEEE/CVF Conference on Computer Vision and Pattern Recognition (CVPR)*. 11799–11809.
- [3] Shaojie Bai, J. Zico Kolter, and Vladlen Koltun. 2018. An Empirical Evaluation of Generic Convolutional and Recurrent Networks for Sequence Modeling. *arXiv:1803.01271* (2018).
- [4] Angel Chang, Thomas Funkhouser, Leonidas Guibas, Pat Hanrahan, Qixing Huang, Zimo Li, Silvio Savarese, Manolis Savva, Shuran Song, Hao Su, Jianxiang Xiao, Li Yi, and Fisher Yu. 2015. ShapeNet: An Information-Rich 3D Model Repository. *arXiv preprint arXiv:1512.03012* (2015).
- [5] R. Q. Charles, H. Su, M. Kaichun, and L. J. Guibas. 2017. PointNet: Deep Learning on Point Sets for 3D Classification and Segmentation. In *Proc. IEEE/CVF Conference on Computer Vision and Pattern Recognition (CVPR)*. 77–85.
- [6] Guangyan Chen, Meiling Wang, Yi Yang, Kai Yu, Li Yuan, and Yufeng Yue. 2023. PointGPT: Auto-regressively Generative Pre-training from Point Clouds. In *Proc. Advances in Neural Information Processing Systems (NeurIPS)*, A. Oh, T. Naumann, A. Globerson, K. Saenko, M. Hardt, and S. Levine (Eds.), Vol. 36. Curran Associates, Inc., 29667–29679.
- [7] Yuwei Cheng, Jingran Su, Mengxin Jiang, and Yimin Liu. 2022. A Novel Radar Point Cloud Generation Method for Robot Environment Perception. *IEEE Transactions on Robotics* 38, 6 (2022), 3754–3773.
- [8] François Chollet. 2017. Xception: Deep Learning with Depthwise Separable Convolutions. In *Proc. IEEE/CVF Conference on Computer Vision and Pattern Recognition (CVPR)*. 1800–1807.
- [9] David Conde, Jesús Balado, Mario Soillán, Joaquín Martínez, and Pedro Arias. 2025. LiDAR Data Processing for Digitization of the Castro of Santa Trega and Integration in Unreal Engine 5. *International Journal of Architectural Heritage* 19, 1 (2025), 131–151.
- [10] Mingyue Cui, Junhua Long, Mingjian Feng, Boyang Li, and Huang Kai. 2023. OctFormer: Efficient Octree-Based Transformer for Point Cloud Compression with Local Enhancement. In *Proc. AAAI Conference on Artificial Intelligence (AAAI)*, Vol. 37. 470–478.
- [11] Marco Cuturi, Olivier Teboul, and Jean-Philippe Vert. 2019. *Differentiable ranks and sorting using optimal transport*. Curran Associates Inc., Red Hook, NY, USA.
- [12] Jifeng Dai, Haozhi Qi, Yuwen Xiong, Yi Li, Guodong Zhang, Han Hu, and Yichen Wei. 2017. Deformable Convolutional Networks. In *Proc. IEEE/CVF International Conference on Computer Vision (ICCV)*. 764–773.
- [13] Runpei Dong et al. 2023. Autoencoders as Cross-Modal Teachers: Can Pretrained 2D Image Transformers Help 3D Representation Learning?. In *Proc. International Conference on Learning Representations (ICLR)*.
- [14] Martin Engilberge, Louis Chevallier, Patrick Pérez, and Matthieu Cord. 2019. SoDeep: A Sorting Deep Net to Learn Ranking Loss Surrogates. In *Proc. IEEE/CVF Conference on Computer Vision and Pattern Recognition (CVPR)*. 10784–10793.
- [15] Daniel Garrido, Rui Rodrigues, A. Augusto Sousa, Joao Jacob, and Daniel Castro Silva. 2021. Point Cloud Interaction and Manipulation in Virtual Reality. In *2021 5th International Conference on Artificial Intelligence and Virtual Reality (AIVR)* (Kumamoto, Japan) (AIVR 2021). Association for Computing Machinery, New York, NY, USA, 15–20.
- [16] Albert Gu and Tri Dao. 2024. Mamba: Linear-Time Sequence Modeling with Selective State Spaces. In *First Conference on Language Modeling*.
- [17] Albert Gu, Karan Goel, and Christopher Ré. 2022. Efficiently Modeling Long Sequences with Structured State Spaces. In *Proc. International Conference on Learning Representations (ICLR)*.
- [18] Albert Gu, Isys Johnson, Karan Goel, Khaled Saab, Tri Dao, Atri Rudra, and Christopher Ré. 2021. Combining Recurrent, Convolutional, and Continuous-time Models with Linear State Space Layers. In *Proc. Advances in Neural Information Processing Systems (NeurIPS)*, M. Ranzato, A. Beygelzimer, Y. Dauphin, P.S. Liang, and J. Wortman Vaughan (Eds.), Vol. 34. Curran Associates, Inc., 572–585.
- [19] Xu Han, Yuan Tang, Zhaoxuan Wang, and Xianzhi Li. 2024. Mamba3D: Enhancing Local Features for 3D Point Cloud Analysis via State Space Model. In *Proc. ACM International Conference on Multimedia (ACM MM)*. ACM, 4995–5004.
- [20] Jie Hu, Li Shen, and Gang Sun. 2018. Squeeze-and-Excitation Networks. In *Proc. IEEE/CVF Conference on Computer Vision and Pattern Recognition (CVPR)*. 7132–7141.
- [21] Tao Huang, Xiaohuan Pei, Shan You, Fei Wang, Chen Qian, and Chang Xu. [n. d.]. LocalMamba: Visual State Space Model with Windowed Selective Scan. In *Proc. European Conference on Computer Vision (ECCV)* (Cham, 2025), Alessio Del Bue, Cristian Canton, Jordi Pont-Tuset, and Tatiana Tommasi (Eds.). Springer Nature Switzerland, 12–22.
- [22] Alexander Kolesnikov, Alexey Dosovitskiy, Dirk Weissenborn, Georg Heigold, Jakob Uszkoreit, Lucas Beyer, Matthias Minderer, Mostafa Dehghani, Neil Houlsby, Sylvain Gelly, Thomas Unterthiner, and Xiaohua Zhai. 2021. An Image is Worth 16x16 Words: Transformers for Image Recognition at Scale. In *Proc. International Conference on Learning Representations (ICLR)*.
- [23] Dengao Li, Zhichao Gao, Shufeng Hao, Ziyou Xun, Jiajian Song, Jie Cheng, and Junmin Zhao. 2025. E-Mamba: An efficient Mamba point cloud analysis method with enhanced feature representation. *Neurocomputing* 639 (2025), 130201.
- [24] Zhuoyuan Li, Yubo Ai, Jiahao Lu, ChuXin Wang, Jiacheng Deng, Hanzhi Chang, Yanzhe Liang, Wenfei Yang, Shifeng Zhang, and Tianzhu Zhang. 2025. Pamba: Enhancing Global Interaction in Point Clouds via State Space Model. In *Proc. AAAI Conference on Artificial Intelligence (AAAI)*, Vol. 39. 5092–5100.
- [25] Dingkan Liang, Xin Zhou, Wei Xu, Xingkui Zhu, Zhikang Zou, Xiaoqing Ye, Xiao Tan, and Xiang Bai. 2024. PointMamba: A Simple State Space Model for Point Cloud Analysis. In *Proc. Advances in Neural Information Processing Systems (NeurIPS)*, Vol. 37. Curran Associates, Inc., 32653–32677.
- [26] Sohee Lim, Minwoo Shin, and Joonki Paik. 2022. Point Cloud Generation Using Deep Adversarial Local Features for Augmented and Mixed Reality Contents. *IEEE Transactions on Consumer Electronics* 68, 1 (2022), 69–76.
- [27] Zhi-Hao Lin, Sheng-Yu Huang, and Yu-Chiang Frank Wang. 2020. Convolution in the Cloud: Learning Deformable Kernels in 3D Graph Convolution Networks for Point Cloud Analysis. In *Proc. IEEE/CVF Conference on Computer Vision and Pattern Recognition (CVPR)*. 1797–1806.
- [28] Bin Liu, Chunyang Wang, Xuelian Liu, Bo Xiao, and Guan Xi. 2025. HyMamba: Mamba with Hybrid Geometry-Feature Coupling for Efficient Point Cloud Classification. *arXiv preprint arXiv:2505.11099v2* (2025).
- [29] Leiye Liu et al. 2025. DefMamba: Deformable Visual State Space Model. In *Proc. IEEE/CVF Conference on Computer Vision and Pattern Recognition (CVPR)*. 8838–8847.
- [30] Yahui Liu, Bin Tian, Yisheng Lv, Lingxi Li, and Fei-Yue Wang. 2024. Point Cloud Classification Using Content-Based Transformer via Clustering in Feature Space. *IEEE/CAA Journal of Automatic Sinica* 11, 1 (2024), 231.
- [31] Yue Liu, Yunjie Tian, Yuzhong Zhao, Hongtian Yu, Lingxi Xie, Yaowei Wang, Qixiang Ye, Jianbin Jiao, and Yunfan Liu. 2024. VMamba: Visual State Space Model. In *Proc. Advances in Neural Information Processing Systems (NeurIPS)*, A. Globerson, L. Mackey, D. Belgrave, A. Fan, U. Paquet, J. Tomczak, and C. Zhang (Eds.), Vol. 37. Curran Associates, Inc., 103031–103063.
- [32] Zhijian Liu, Xinyu Yang, Haotian Tang, Shang Yang, and Song Han. 2023. FlatFormer: Flattened Window Attention for Efficient Point Cloud Transformer. In *Proc. IEEE/CVF Conference on Computer Vision and Pattern Recognition (CVPR)*. 1200–1211.
- [33] Dening Lu, Kyle Gao, Jonathan Li, Dedong Zhang, and Linlin Xu. 2025. Exploring Token Serialization for Mamba-Based LiDAR Point Cloud Segmentation. *IEEE Transactions on Geoscience and Remote Sensing* 63 (2025), 1–14.
- [34] Dening Lu, Linlin Xu, Jun Zhou, Kyle Gao, Zheng Gong, and Dedong Zhang. 2025. 3D-UMamba: 3D U-Net with state space model for semantic segmentation of multi-source LiDAR point clouds. *International Journal of Applied Earth Observation and Geoinformation* 136 (2025), 104401.
- [35] Yatian Pang, Wenxiao Wang, Francis E. H. Tay, Wei Liu, Yonghong Tian, and Li Yuan. 2022. Masked Autoencoders for Point Cloud Self-supervised Learning. In *Proc. European Conference on Computer Vision (ECCV)*. Cham, 604–621.
- [36] Adam Paszke, Sam Gross, Francisco Massa, Adam Lerer, James Bradbury, Gregory Chanan, Trevor Killeen, Zeming Lin, Natalia Gimelshein, Luca Antiga, Alban Desmaison, Andreas Kopf, Edward Yang, Zachary DeVito, Martin Raison, Alykhan Tejani, Sasank Chilamkurthy, Benoit Steiner, Lu Fang, Junjie Bai, and Soumith Chintala. 2019. PyTorch: An Imperative Style, High-Performance Deep

- Learning Library. In *Advances in Neural Information Processing Systems*, H. Wallach, H. Larochelle, A. Beygelzimer, F. d'Alché-Buc, E. Fox, and R. Garnett (Eds.), Vol. 32. Proc. Advances in Neural Information Processing Systems (NeurIPS).
- [37] Charles Ruizhongtai Qi, Li Yi, Hao Su, and Leonidas J Guibas. 2017. PointNet++: Deep Hierarchical Feature Learning on Point Sets in a Metric Space. In *Proc. Advances in Neural Information Processing Systems (NeurIPS)*, Vol. 30. Curran Associates, Inc.
- [38] Guocheng Qian, Yuchen Li, Houwen Peng, Jinjie Mai, Hasan Hammoud, Mohamed Elhoseiny, and Bernard Ghanem. 2022. PointNetXt: Revisiting PointNet++ with Improved Training and Scaling Strategies. In *Proc. Advances in Neural Information Processing Systems (NeurIPS)*, Vol. 35. 23192–23204.
- [39] Kanglin Qu, Pan Gao, Qun Dai, and Yuanhao Sun. 2025. HydraMamba: Multi-Head State Space Model for Global Point Cloud Learning. In *Proc. ACM International Conference on Multimedia (ACM MM)*. 333–342.
- [40] K. L. Qu, P. Gao, Q. Dai, Z. Z. Ye, R. Ye, and Y. H. Sun. 2026. CloudMamba: Grouped Selective State Spaces for Point Cloud Analysis. In *Proc. AAAI Conference on Artificial Intelligence (AAAI)*, Singapore EXPO.
- [41] Hugues Thomas, Charles R. Qi, Jean-Emmanuel Deschaud, Beatriz Marcotequi, François Goulette, and Leonidas Guibas. 2019. KPConv: Flexible and Deformable Convolution for Point Clouds. In *Proc. IEEE/CVF International Conference on Computer Vision (ICCV)*. 6410–6419.
- [42] Mikaela Angelina Uy, Quang-Hieu Pham, Binh-Son Hua, Thanh Nguyen, and Sai-Kit Yeung. 2019. Revisiting Point Cloud Classification: A New Benchmark Dataset and Classification Model on Real-World Data. In *Proc. IEEE/CVF International Conference on Computer Vision (ICCV)*. 1588–1597.
- [43] Ashish Vaswani, Noam Shazeer, Niki Parmar, Jakob Uszkoreit, Llion Jones, Aidan N. Gomez, Łukasz Kaiser, and Illia Polosukhin. 2017. Attention is all you need. In *Proc. Advances in Neural Information Processing Systems (NeurIPS)* (Long Beach, California, USA) (NIPS'17). Curran Associates Inc., Red Hook, NY, USA, 6000–6010.
- [44] Chuxin Wang et al. 2025. StruMamba3D: Exploring Structural Mamba for Self-supervised Point Cloud Representation Learning. *arXiv preprint arXiv:2506.21541*.
- [45] H. Wang, Q. Liu, X. Yue, J. Lasenby, and M. J. Kusner. 2021. Unsupervised Point Cloud Pre-training via Occlusion Completion. In *Proc. IEEE/CVF International Conference on Computer Vision (ICCV)*. 9762–9772.
- [46] Peng-Shuai Wang. 2023. OctFormer: Octree-based Transformers for 3D Point Clouds. *ACM Transactions on Graphics* 42, 4, Article 155 (July 2023), 11 pages.
- [47] Xinjie Wang, Yifan Zhang, Ting Liu, Xinpui Liu, Ke Xu, Jianwei Wan, Yulan Guo, and Hanyun Wang. 2025. TopNet: Transformer-Efficient Occupancy Prediction Network for Octree-Structured Point Cloud Geometry Compression. In *Proc. IEEE/CVF Conference on Computer Vision and Pattern Recognition (CVPR)*. 27305–27314.
- [48] Yue Wang, Yongbin Sun, Ziwei Liu, Sanjay E. Sarma, Michael M. Bronstein, and Justin M. Solomon. 2019. Dynamic Graph CNN for Learning on Point Clouds. *ACM Transactions on Graphics* 38, 5, Article 146 (Oct. 2019), 12 pages.
- [49] Wenxuan Wu, Zhongang Qi, and Li Fuxin. 2019. PointConv: Deep Convolutional Networks on 3D Point Clouds. In *Proc. IEEE/CVF Conference on Computer Vision and Pattern Recognition (CVPR)*. 9613–9622.
- [50] Xiaoyang Wu, Li Jiang, Peng-Shuai Wang, Zhijian Liu, Xihui Liu, Yu Qiao, Wanli Ouyang, Tong He, and Hengshuang Zhao. 2024. Point Transformer V3: Simpler, Faster, Stronger. In *Proc. IEEE/CVF Conference on Computer Vision and Pattern Recognition (CVPR)*. 4840–4851.
- [51] Xiaoyang Wu, Yixing Lao, Li Jiang, Xihui Liu, and Hengshuang Zhao. 2022. Point transformer V2: Grouped Vector Attention and Partition-based Pooling. In *Proc. Advances in Neural Information Processing Systems (NeurIPS)*.
- [52] Zhirong Wu, Shuran Song, Aditya Khosla, Fisher Yu, Linguang Zhang, Xiaoou Tang, and Jianxiong Xiao. 2015. 3D ShapeNets: A deep representation for volumetric shapes. In *Proc. IEEE/CVF Conference on Computer Vision and Pattern Recognition (CVPR)*. 1912–1920.
- [53] Zhuofan Xia, Xuran Pan, Shiji Song, Li Erran Li, and Gao Huang. 2022. Vision Transformer with Deformable Attention. In *Proc. IEEE/CVF Conference on Computer Vision and Pattern Recognition (CVPR)*. 4784–4793.
- [54] Chenhongyi Yang, Zehui Chen, Miguel Espinosa, Linus Ericsson, Zhenyu Wang, Jiaming Liu, and Elliot J. Crowley. 2024. PlainMamba: Improving Non-Hierarchical Mamba in Visual Recognition. In *35th British Machine Vision Conference (BMVC)*.
- [55] Yulong Yang, Tianzhou Xun, Kuangrong Hao, Bing Wei, and Xue-song Tang. [n. d.]. Grid Mamba: Grid State Space Model for large-scale point cloud analysis. *Neurocomputing* 636 ([n. d.]), 129985.
- [56] Weihao Yu and Xinchao Wang. 2025. MambaOut: Do We Really Need Mamba for Vision?. In *Proc. IEEE/CVF Conference on Computer Vision and Pattern Recognition (CVPR)*. 4484–4496.
- [57] Xumin Yu, Lulu Tang, Yongming Rao, Tiejun Huang, Jie Zhou, and Jiwen Lu. 2022. Point-BERT: Pre-training 3D Point Cloud Transformers with Masked Point Modeling. In *Proc. IEEE/CVF Conference on Computer Vision and Pattern Recognition (CVPR)*. 19291–19300.
- [58] Kang Zeng, Hao Shi, Jiacheng Lin, Siyu Li, Jintao Cheng, Kaiwei Wang, Zhiyong Li, and Kailun Yang. 2024. MambaMOS: LiDAR-based 3D Moving Object Segmentation with Motion-aware State Space Model. *arXiv preprint arXiv:2404.12794* (2024).
- [59] Yaohua Zha, Huizhen Ji, Jimmin Li, Rongsheng Li, Tao Dai, Bin Chen, Zhi Wang, and Shu-Tao Xia. 2024. Towards Compact 3D Representations via Point Feature Enhancement Masked Autoencoders. In *Proc. AAAI Conference on Artificial Intelligence (AAAI)*, Vol. 38. 6962–6970.
- [60] Guowen Zhang, Lue Fan, Chenhang He, Zhen Lei, Zhaoxiang Zhang, and Lei Zhang. 2024. Voxel Mamba: group-free state space models for point cloud based 3D object detection. In *Proc. Advances in Neural Information Processing Systems (NeurIPS)* (Vancouver, BC, Canada) (NIPS '24). Curran Associates Inc., Red Hook, NY, USA, Article 2590, 21 pages.
- [61] Lunjun Zhang, Anqi Joyce Yang, Yuwen Xiong, Sergio Casas, Bin Yang, Mengye Ren, and Raquel Urtasun. 2023. Towards Unsupervised Object Detection from LiDAR Point Clouds. In *Proc. IEEE/CVF Conference on Computer Vision and Pattern Recognition (CVPR)*. 9317–9328.
- [62] Tao Zhang et al. 2025. Point Cloud Mamba: Point Cloud Learning via State Space Model. In *Proc. AAAI Conference on Artificial Intelligence (AAAI)*, Vol. 39. 10121–10130.
- [63] Xiangdong Zhang, Shaofeng Zhang, and Junchi Yan. 2025. Towards More Diverse and Challenging Pre-training for Point Cloud Learning: Self-Supervised Cross Reconstruction with Decoupled Views. In *Proc. IEEE/CVF International Conference on Computer Vision (ICCV)*.
- [64] Xiangyu Zhang, Xinyu Zhou, Mengxiao Lin, and Jian Sun. 2018. ShuffleNet: An Extremely Efficient Convolutional Neural Network for Mobile Devices. In *Proc. IEEE/CVF Conference on Computer Vision and Pattern Recognition (CVPR)*. 6848–6856.
- [65] Hengshuang Zhao, Li Jiang, Jiaya Jia, Philip Torr, and Vladlen Koltun. 2021. Point Transformer. In *Proc. IEEE/CVF International Conference on Computer Vision (ICCV)*. 16239–16248.
- [66] Zixiang Zhou, Xiangchen Zhao, Yu Wang, Panqu Wang, and Hassan Foroosh. 2022. CenterFormer: Center-based Transformer for 3D Object Detection. In *Proc. European Conference on Computer Vision (ECCV)*. 496–513.
- [67] Lianghui Zhu, Bencheng Liao, Qian Zhang, Xinlong Wang, Wenyu Liu, and Xinggang Wang. 2024. Vision Mamba: Efficient Visual Representation Learning with Bidirectional State Space Model. In *Proc. International Conference on Machine Learning (ICML)*, Vol. 235. 62429–62442.

## A Analysis of GDR Differentiability

In this section, we analyze the Gaussian weights and their derivatives with respect to the offset index values  $s_i$  to characterize the behavior of Gaussian-based Differentiable Reordering (GDR).

GDR restricts the candidate indices for token  $i$  to a fixed local index window  $\Omega(i)$  centered at its base index  $I_i$ , with cardinality  $K_i = |\Omega(i)| \leq K_t$ . For theoretical clarity, we omit the term  $\varepsilon$ , which is used only for numerical stability in implementation. The weighting function is defined as:

$$W_{ij}^{(t)} = \frac{\exp\left(-\frac{(s_i - I_j)^2}{2\sigma_t^2}\right)}{\sum_{l \in \Omega(i)} \exp\left(-\frac{(s_i - I_l)^2}{2\sigma_t^2}\right)}, \quad j \in \Omega(i) \quad (17)$$

where  $\sigma_t$  is the Gaussian scale parameter in the sequential domain, and  $s_i = I_i + \Delta t_i$  denotes the offset index value of the  $i$ -th token after applying the learned offset  $\Delta t_i$ .

To analyze gradient propagation, the first-order derivative of  $W_{ij}^{(t)}$  with respect to  $s_i$  is given by:

$$\frac{\partial W_{ij}^{(t)}}{\partial s_i} = \frac{W_{ij}^{(t)}}{\sigma_t^2} \left( I_j - \sum_{l \in \Omega(i)} W_{il}^{(t)} I_l \right), \quad j \in \Omega(i) \quad (18)$$

For  $j \notin \Omega(i)$ ,  $W_{ij}^{(t)} = 0$  by definition, and thus its derivative with respect to  $s_i$  is also zero. We analyze three cases within the local candidate set  $\Omega(i)$ :  $\sigma_t \rightarrow +\infty$ ,  $\sigma_t > 0$ , and  $\sigma_t \rightarrow 0^+$ .

### A.1 Case 1: Analysis of $\sigma_t \rightarrow +\infty$

As  $\sigma_t \rightarrow +\infty$ , all exponential terms within the local window  $\Omega(i)$  converge to 1, yielding:

$$\lim_{\sigma_t \rightarrow +\infty} W_{ij}^{(t)} = \frac{1}{K_i}, \quad \lim_{\sigma_t \rightarrow +\infty} \frac{\partial W_{ij}^{(t)}}{\partial s_i} = 0 \quad (19)$$

In this case, GDR degenerates into local average pooling over the candidate window  $\Omega(i)$ , and the gradients with respect to  $s_i$  vanish.

### A.2 Case 2: Analysis of $\sigma_t > 0$

When  $\sigma_t$  is finite and positive, each local weight  $W_{ij}^{(t)}$  is infinitely differentiable with respect to  $s_i$  for all  $j \in \Omega(i)$ . Since  $W_{ij}^{(t)} \in (0, 1)$  and Eq. (18) is continuous in  $s_i$  over the  $\Omega(i)$ , the derivative is also continuous and remains bounded with respect to  $s_i$ .

In this case, GDR performs a continuously differentiable local reassignment mapping operation, which supports stable backpropagation through  $s_i$ .

### A.3 Case 3: Analysis of $\sigma_t \rightarrow 0^+$

According to Eq. (17), the relative distances between  $s_i$  and the candidate indices determine the weights, leading to two scenarios:  $s_i$  has a unique nearest candidate, or it is equidistant to two candidates.

Let  $d_{\min}^2 = \min_{l \in \Omega(i)} (s_i - I_l)^2$  and define the active index set  $\mathcal{T}_i = \{j \in \Omega(i) | (s_i - I_j)^2 = d_{\min}^2\}$  with cardinality  $m_i = |\mathcal{T}_i|$ . The

Gaussian kernel can then be rewritten as:

$$\begin{aligned} \mathcal{W}(s_i - I_j; \sigma_t) &= \exp\left(-\frac{(s_i - I_j)^2}{2\sigma_t^2}\right) \\ &= \exp\left(-\frac{d_{\min}^2}{2\sigma_t^2}\right) \cdot \exp\left(-\frac{(s_i - I_j)^2 - d_{\min}^2}{2\sigma_t^2}\right) \end{aligned} \quad (20)$$

For all  $j \in \mathcal{T}_i$ , the second term equals 1. For  $j \notin \mathcal{T}_i$ , it decays exponentially. Substituting into the normalized weight yields:

$$W_{ij}^{(t)} = \frac{\exp\left(-\frac{(s_i - I_j)^2 - d_{\min}^2}{2\sigma_t^2}\right)}{\sum_{l \in \mathcal{T}_i} 1 + \sum_{l \notin \mathcal{T}_i} \exp\left(-\frac{(s_i - I_l)^2 - d_{\min}^2}{2\sigma_t^2}\right)} \quad (21)$$

**Case 3a:  $s_i$  has a unique nearest candidate  $I_k$  within  $\Omega(i)$ .** When  $s_i$  has a unique nearest local index  $I_k$  within  $\Omega(i)$ , we have  $\mathcal{T}_i = \{k\}$  and  $m_i = 1$ . The non-minimum terms vanish exponentially, yielding:

$$\lim_{\sigma_t \rightarrow 0^+} W_{ij}^{(t)} = \begin{cases} 1, & j = k \\ 0, & j \neq k \end{cases} \quad (22)$$

For the derivative, both  $W_{ij}^{(t)}$  and its weighted sum decay exponentially, leading to:

$$\lim_{\sigma_t \rightarrow 0^+} \frac{\partial W_{ij}^{(t)}}{\partial s_i} = 0, \quad j \in \Omega(i) \quad (23)$$

In this scenario, the weight deterministically assigns  $s_i$  to its nearest local index  $I_k$ , and the gradient vanishes, indicating that GDR degenerates into deterministic local reassignment within  $\Omega(i)$ .

**Case 3b:  $s_i$  is equidistant to two local indices.** In this scenario,  $m_i = 2$ , and all  $j \in \mathcal{T}_i$  have  $(s_i - I_j)^2 = d_{\min}^2$ , while the other indices have larger distances. As  $\sigma_t \rightarrow 0^+$ , the minor terms in the denominator vanish, leading to:

$$\lim_{\sigma_t \rightarrow 0^+} W_{ij}^{(t)} = \begin{cases} \frac{1}{m_i}, & j \in \mathcal{T}_i \\ 0, & j \notin \mathcal{T}_i \end{cases} \quad (24)$$

For the derivative, when  $j \notin \mathcal{T}_i$ ,  $W_{ij}^{(t)}$  decays exponentially, so the derivative tends to 0. For  $j \in \mathcal{T}_i$ , the derivative is given by:

$$\frac{\partial W_{ij}^{(t)}}{\partial s_i} = \frac{1}{m_i \sigma_t^2} (I_j - \bar{I}_{\mathcal{T}_i}), \quad \bar{I}_{\mathcal{T}_i} = \frac{1}{m_i} \sum_{l \in \mathcal{T}_i} I_l \quad (25)$$

where  $\bar{I}_{\mathcal{T}_i}$  denotes the mean index of  $\mathcal{T}_i$ . Since  $m_i = 2$  and the two indices are distinct,  $I_j - \bar{I}_{\mathcal{T}_i} \neq 0$  for each  $j \in \mathcal{T}_i$ . Therefore:

$$\lim_{\sigma_t \rightarrow 0^+} \frac{\partial W_{ij}^{(t)}}{\partial s_i} = \begin{cases} 0, & j \notin \mathcal{T}_i \\ +\infty, & j \in \mathcal{T}_i, I_j > \bar{I}_{\mathcal{T}_i} \\ -\infty, & j \in \mathcal{T}_i, I_j < \bar{I}_{\mathcal{T}_i} \end{cases} \quad (26)$$

In this scenario, the weights are evenly distributed across the equidistant local candidates, while the derivatives with respect to  $s_i$  diverge. However, even a slight perturbation of  $s_i$  breaks the symmetry and restores finite gradients, as in Case 3a. Consequently, the model is unlikely to remain in such equidistant states during training.

Overall, GDR maps each offset index value  $s_i$  to a probabilistic assignment over the local candidate window  $\Omega(i)$ , which provides

a continuous and differentiable relaxation of local discrete reassignment in the index space. For any finite  $\sigma_t > 0$ , the weighting function remains smooth and differentiable with respect to  $s_i$ , enabling stable gradient propagation. As  $\sigma_t \rightarrow 0^+$ , the mapping converges to nearest-candidate selection within  $\Omega(i)$ , i.e., deterministic local reassignment. Conversely, as  $\sigma_t \rightarrow \infty$ , GDR degenerates into local average pooling and loses its reordering capability. Hence,  $\sigma_t$  is typically chosen to be relatively small in practice, and an  $\varepsilon$  term is introduced for numerical stability.

## B More Experimental Results

### B.1 More Implementation Details

Following PointMamba [25] and Mamba3D [19], we adopt the masked pre-training strategy of Point-MAE [35], using a masking ratio of 60% and rotation augmentation during pre-training. Table 6 summarizes the detailed hyperparameter settings for pre-training, classification, and part segmentation. For both classification and part segmentation, we use the cross-entropy loss. During training,  $\sigma_t$  is initialized to 0.2 and converges stably without exhibiting gradient collapse.

### B.2 Scene-level semantic segmentation.

We evaluate scene-level semantic segmentation on the S3DIS dataset [1]. Following the common Area 5 split protocol [24, 50, 62], we train on Areas 1–4 and Area 6, and report results on Area 5. For the S3DIS dataset [1], we follow the training pipeline of PCM [62] and use a separate configuration, with the hidden dimension set to 96 and the drop path rate set to 0.1. We use AdamW with an initial learning rate of  $1e-4$ , weight decay of 0.05, 5 warmup epochs, a batch size of 4, and 128 training epochs.

As shown in Tab. 7, DM3D achieves 66.3% mIoU and 71.0% mAcc, surpassing Point-PQAE [63] by 4.9 mIoU and PointGPT-L [6] by 4.1 mIoU. Although PTv3 [50] and Pamba [24] achieve higher mIoU, DM3D still yields solid results as a generic architecture without task-specific components.

### B.3 Additional Ablation Studies

*Effect of local candidate size  $K_t$ .*  $K_t$  controls the local candidate window in GDR. Smaller values limit the flexibility of local reordering, while larger ones may introduce redundant candidates. As shown in Table 8, performance gradually improves as  $K_t$  increases from 5 to 9, and the best results are achieved at  $K_t = 9$ . When  $K_t$  is further increased to 11, the gain saturates and drops slightly, indicating that an overly large candidate window is not beneficial.

*Effect of resampling neighborhood size  $K_r$ .* Since the learned offsets are bounded, deformable spatial resampling (DSR) is intended to perform deformation within a local neighborhood rather than completely rebuilding the neighborhood graph. Therefore, we reuse the local neighborhood constructed in local context feature aggregation (LCFA) for resampling, instead of re-running neighbor search after applying  $\Delta p$ . As shown in Table 9, this design achieves almost the same as re-querying the neighbors after deformation. This indicates that a fixed local neighborhood is sufficient. In contrast, re-querying after  $\Delta p$  introduces an additional ball query and

**Table 6: Implementation details and hyperparameter settings for pre-training and different downstream tasks. S&T: Scale&Translation.**

Config	Pre-training	Classification	Part Seg
Setting	ShapeNet	MN40/ScanNN	ShapeNetPart
Optimizer	AdamW	AdamW	AdamW
Learning rate	1e-3	5e-4	2e-4
Weight decay	0.05	0.05	0.05
Scheduler	CosLR	CosLR	CosLR
Warmup epochs	10	10	10
Drop path rate	0.1	0.1	0.3
Training epochs	300	300	300
Batch size	64	32	32
Input points	1024	1024/2048	2048
Hidden dim ( $D$ )	384	384	384
Stage layers ( $T$ )	12	12	12
FPS samples ( $N$ )	64	128	128
KNN neighbors ( $K$ )	32	32	16
Ball query radius ( $r$ )	0.25	0.2/0.25	0.25
OffsetNet kernel size	5	5	5
SFC	Hilbert	Hilbert	Hilbert
LCFA and DSR $K_r$	4	4	4
GDR $K_t$	9	9	9
DSR $\sigma_s$	1	1	1
GDR $\sigma_t$	0.2	0.2	0.2
Augmentation	Rotation	S&T / Rotation	Scale&Center

**Table 7: Scene-level semantic segmentation on S3DIS. We report mean accuracy (mAcc) and mean IoU (mIoU).**

Reference	Method	mAcc (%)	mIoU (%)
NeurIPS 17	PointNet++ [37]	67.1	53.5
CVPR 22	Point-BERT [57]	70.3	60.8
ECCV 22	Point-MAE [35]	69.9	60.8
NeurIPS 23	PointGPT-L [6]	70.6	62.2
ICLR 23	ACT [13]	71.1	61.2
CVPR 24	PTv3 [50]	<b>78.9</b>	73.4
ICCV 25	Point-PQAE [63]	70.6	61.4
AAAI 25	Pamba [24]	-	<b>73.5</b>
AAAI 25	PCM [62]	-	63.4
	DM3D	71.0	66.3

gather operations. We expect the resulting accuracy gain to be marginal compared with the increase in computation. Hence, we adopt neighbor reuse in DSR as a better accuracy-efficiency trade-off.

The smaller  $K_r$  leads to insufficient local aggregation, whereas a larger  $K_r$  tends to introduce irrelevant points. Among all settings,  $K_r = 4$  achieves the best trade-off. Therefore, we reuse the local neighborhood with  $K_r = 4$  in both LCFA and DSR.

*Reliability of neighborhood reuse.* To examine the concern that spatial offsets may move points outside the original ball query neighborhood, we report statistics of the spatial offset magnitudes  $\|\Delta p\|_2$  in Tab. 10. These statistics are computed from 256 samples per dataset, with 128 points per sample, yielding 32,768 point offsets for each dataset.

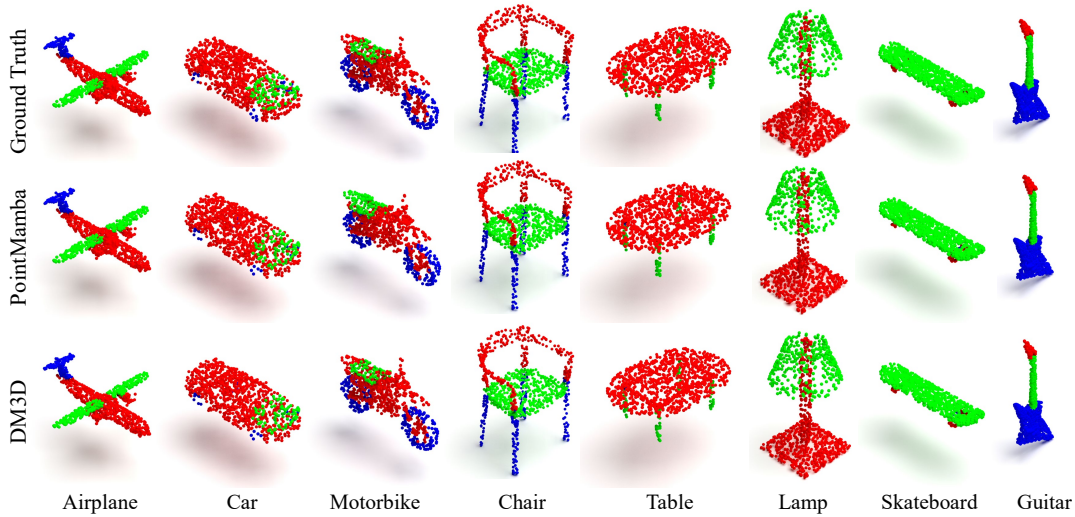


Figure 6: Qualitative part segmentation results on ShapeNetPart from DM3D and PointMamba.

Table 8: Ablation on parameters  $K_l$ .  $K_l$ : the number of local candidate indexes.

$K_l$ Value	OBJ_ONLY	PB_T50_RS
5	91.49	90.31
7	91.54	90.77
9	<b>91.74</b>	<b>90.83</b>
11	91.37	90.80

Table 9: Ablation on neighborhood size  $K_r$  in LCFA and DSR.

Reuse neighbors	$K_r$ value	OBJ_ONLY	PB_T50_RS
$\times$	4	91.80	90.71
$\checkmark$	2	91.49	89.53
	3	91.54	89.65
	4	<b>91.74</b>	<b>90.83</b>
	5	91.57	89.78

As shown in Table 10, the 95th percentile of  $\|\Delta p\|_2$  is below  $r$  for all datasets, and the violation rate ( $\|\Delta p\|_2 > r$ ) is consistently below 1%. These results indicate that spatial offsets rarely move points outside their original local neighborhoods, thereby supporting the reliability of neighborhood reuse in DSR. That is, the learned deformation primarily acts as a local geometric refinement rather than reconstructing neighborhoods from scratch.

**Sensitivity to base serialization.** To further evaluate the impact of different base serializations on our deformable mechanism, we compare three initializations: Hilbert, Z-order, and random order.

As shown in Table 11, the deformable variants consistently outperform their base-order counterparts under all initializations, demonstrating that DM3D is not tied to a specific initialization. The

Table 10: Statistics of the spatial offset magnitudes  $\|\Delta p\|_2$  with respect to the ball query radius  $r$ .

Dataset	ModelNet40	OBJ_ONLY	PB_T50_RS
Query radius ( $r$ )	0.2	0.25	0.25
Mean value	0.118	0.130	0.121
95th percentile	0.162	0.200	0.179
Violation count	180	124	26
Violation rate	0.55%	0.38%	0.08%

Table 11: Effect of Base Serialization on DM3D.

Serialization	ModelNet40		PB_T50_RS	
	Base	Deformable	Base	Deformable
Hilbert	92.41	<b>94.01</b>	88.62	<b>90.83</b>
Z-order	91.98	93.85	88.25	90.45
Random	91.12	93.41	87.71	90.03

gains are particularly clear on the more challenging PB\_T50\_RS, where deformable scanning brings stable improvements under all settings. Although the choice of base order still affects the final performance, the relatively narrow gap between different initializations shows that DM3D is not overly reliant on a particular base serialization.

#### B.4 Part segmentation visualization

Fig. 6 presents qualitative comparisons on the ShapeNetPart [4] test set, including Ground Truth (GT), PointMamba [25] predictions, and our DM3D predictions. Compared with PointMamba, DM3D produces cleaner part separation and fewer misclassified points by better preserving local part structure. The enlarged views in Fig. 7 further highlight these differences. On "motorbike", DM3D more

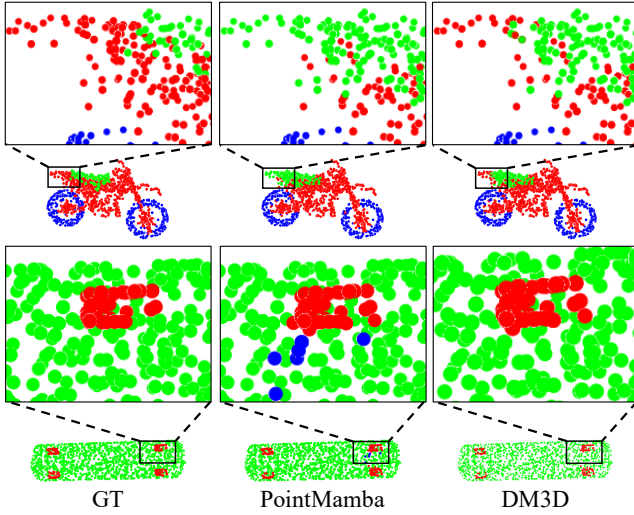


Figure 7: Detailed visualizations of part segmentation results.

accurately distinguishes the seat from the surrounding body components in cluttered local regions, reducing boundary confusion between adjacent parts. On "skateboard", our DM3D produces more compact and accurate wheel regions, whereas PointMamba introduces isolated outliers. These qualitative results further demonstrate the benefit of the proposed deformable scanning for fine-grained part segmentation.

## B.5 Computational Complexity

Let  $B$  and  $N$  denote the batch size and the number of point tokens, respectively. We use  $D$  for the feature dimension,  $K_r$  for the reused local neighborhood size,  $K_t$  for the local candidate window size, and  $G$  for the number of groups in the grouped  $1 \times 1$  convolution in TPF.

The complexity ( $\Delta C$ ) of the additional modules can be summarized as:

$$\Delta C = O(BND [ \underbrace{K_r}_{\text{LCFA+DSR}} + \underbrace{K_t}_{\text{GDR}} + \underbrace{D}_{\text{OffsetNet}} + \underbrace{D/G}_{\text{TPF}} + \underbrace{1}_{\text{CASU}} ]) \quad (27)$$

The LCFA and DSR are both confined to a reused local neighborhood of size  $K_r$ , and their combined cost is  $O(BNDK_r)$ . GDR operates within a local candidate window of size  $K_t$ , contributing  $O(BNDK_t)$ . The dominant convolution costs of OffsetNet and TPF are  $O(BND^2)$  and  $O(BND^2/G)$ , respectively, while CASU adds  $O(BND)$  due to element-wise step-size modulation. Since  $D$ ,  $G$ ,  $K_r$ , and  $K_t$  are fixed by design, the added overhead grows linearly with the sequence length  $N$ .

## C PyTorch-style Pseudocode

We provide simplified PyTorch-style pseudocode for the core proposed modules, including Deformable Scan, Tri-Path Fusion, and the Deformable Mamba Block.

### Algorithm 1: Simplified pseudo-code of Deformable Scan.

```
# Deformable Scan
class DeformableScan(nn.Module):
```

```
def __init__(self, in_channels):
    super().__init__()
    self.semantic_proj = LowRankProjection(
        in_channels)
    self.offset_net = OffsetNet(in_channels)

    self.sigma_s = nn.Parameter(torch.tensor(1.0))
    self.sigma_t = nn.Parameter(torch.tensor(0.2))

def forward(self, coords, feats, base_idx, knn_idx):
    # feats: [B, N, C], coords: [B, N, 3]

    # LCFA
    neighbor_feat=group(feats,knn_idx) #[B,N,K_r,C]
    center_feat = feats.unsqueeze(2) #[B,N,1,C]

    diff_feat = neighbor_feat - center_feat
    mu_m = diff_feat.mean(dim=2)
    mu_d = diff_feat.abs().mean(dim=2)
    f_sem = self.semantic_proj(mu_m.abs() + mu_d)
    f_agg = concat(mu_m + mu_d + alpha * feats,
        f_sem)

    # Offset
    offset = self.offset_net(f_agg) #[B, N, 4]
    delta_p = torch.tanh(offset[... , :3])
    delta_t = torch.tanh(offset[... , 3])

    # DSR
    deformed_coords = coords + delta_p
    neighbor_pos=group(coords,knn_idx) #[B,N,K_r,3]
    dist_s = l2_distance(deformed_coords.unsqueeze(
        2), neighbor_pos)
    w_s = gaussian_weight(dist_s, self.sigma_s)

    f_resampled = weighted_sum(neighbor_feat, w_s)
    gate = torch.sigmoid(feats.norm(dim=-1, keepdim=
        True))
    f_resampled = f_resampled + gate * feats

    # GDR
    s = base_idx.float() + delta_t
    local_idx=local_index_window(base_idx)#[B,N,K_t]
    local_feat = group(f_resampled, local_idx)

    dist_t = s.unsqueeze(-1) - local_idx.float()
    w_t = gaussian_weight(dist_t, self.sigma_t)
    f_reordered = weighted_sum(local_feat, w_t)

    return f_reordered, deformed_coords, s
```

### Algorithm 2: Simplified pseudo-code of the Tri-Path Fusion.

```
# Tri-Path Fusion
class ChannelShuffle(nn.Module):
    def __init__(self, groups):
        super().__init__()
        self.groups = groups
    def forward(self, x):
        batch, channels, length = x.size()
        channels_per_group = channels // self.groups
        x = x.view(batch, self.groups,
            channels_per_group, length)
        x = torch.transpose(x, 1, 2).contiguous()
        return x.view(batch, channels, length)

class TPF(nn.Module):
    def __init__(self, dim):
        super().__init__()
        self.fuse_proj = nn.Conv1d()
        self.channel_shuffle = ChannelShuffle(groups)

    def forward(self, F_f, F_c, F_d):
        w_f = torch.sigmoid(F_f)
        w_c = torch.sigmoid(F_c)
        w_d = torch.sigmoid(F_d)
```

```

F_f = F_f * (w_c + w_d) / 2
F_c = F_c * (w_f + w_d) / 2
F_d = F_d * (w_f + w_c) / 2

F = concat(F_f, F_c, F_d, dim=1)
F = self.fuse_proj(F)
F = self.channel_shuffle(F)
return F

```

---

### Algorithm 3: Simplified pseudo-code of the Deformable Mamba Block.

---

```

# Deformable Mamba Block
class DeformableMambaBlock(nn.Module):
    def __init__(self, dim):
        super().__init__()
        self.in_proj = Linear(dim, inner_dim)
        self.f_ssm = StandardSSM(inner_dim) # F-SSM
        self.c_ssm = BackwardSSM(inner_dim) # C-SSM
        self.d_conv = DepthwiseConv(inner_dim)
        self.d_scan = DeformableScan(inner_dim) # D-SSM
        self.selective_scan = SelectiveSSM(inner_dim)
        self.tpf = TPF(inner_dim)
        self.out_proj = Linear(inner_dim, dim)

    def forward(self, x, coords, base_idx, knn_idx):
        # x: [B, N, C]
        x = self.in_proj(x)

        # F-SSM
        out_f = self.f_ssm(x)
        # C-SSM
        out_c = self.c_ssm(reverse(x))
        out_c = reverse(out_c)
        # D-SSM
        f_def, coords_def, order_def = self.d_scan(
            coords, x, base_idx, knn_idx)
        f_def = self.d_conv(f_def)

        # CASU
        dist = torch.norm(new_coord[:, 1:] - new_coord
           [:, :-1], dim=-1)
        dt = project_step(f_def)
        dt = dt * (1 + torch.tanh(dist)).unsqueeze(1)

        # Tri-path fusion
        out_d = self.selective_scan(f_def, dt)
        out = self.tpf(out_f, out_c, out_d)
        out = self.out_proj(out)

        return out, coords_def, order_def

```

---